8370 *Macromolecules* **2009**, *42*, 8370–8384
DOI: 10.1021/ma9011158

Macromolecules
ARTICLE

Rheology and Microstructure of Entangled Polymer Nanocomposite Melts

Benjamin J. Anderson[†] and Charles F. Zukoski*

Department of Chemical and Biomolecular Engineering, University of Illinois at Urbana−Champaign, 600 South Mathews Ave, Urbana, Illinois 61801. [†] *Present address: Sandia National Laboratories, Albuquerque, NM 87185-1245.*

Received May 22, 2009; Revised Manuscript Received August 28, 2009

ABSTRACT: The rheology and microstructure of 44 nm diameter silica particles suspended in entangled poly(ethylene oxide) (PEO) melts are studied through measurement of filled melt viscosity and X-ray scattering measurement of interparticle structure factors, $S(q,\phi_c)$, where q is the scattering vector and ϕ_c is the silica volume fraction. The particles have a similar refractive index to PEO which minimizes van der Waals attractions acting between particles. The introduction of particles causes an elevation in the viscosity of the nanocomposite melt more than would be expected of particles merely interacting with hard core repulsions. Further addition of particles causes a rise in the elastic and viscous moduli. The rheological characterization of these nanocomposite melts is discussed in terms of several critical particle volume fractions that result from confinement of polymer, adsorption of polymer segments to the particle surface, and overlap and entanglement of adsorbed polymer as the particle volume fraction is increased. Characterization of the particle microstructure shows that the association of the polymer with the particles drives the particles to structure more than would be expected of particles with interactions governed merely by hard core repulsions. Particles show signs of instability in the polymer melt at a common elevated volume fraction independent of polymer molecular weight.

I. Introduction

When particles are introduced to high molecular weight polymers, the resulting nanocomposite grows in elasticity with a typically strong elevation in the low frequency linear viscoelastic moduli signaling a lengthening of the terminal relaxation time.[1−5] At strains substantially below where the neat polymer shows nonlinearity in its mechanical response, the nanocomposite becomes nonlinear.[1−3,5−7] The origin of these phenomena is poorly understood. Explanations for mechanical enhancement include confinement enhanced entanglements,[8,9] trapped entanglements,[7] polymer bridging,[4] and particle phase separation leading to gelation.[10] In the study of nanocomposites, the state of the dispersion is not always documented, adding to difficulties in understanding what controls nanocomposite mechanical properties. The limited ability to explain the observed phenomena hinders nanocomposite design and processing.

Recent equilibrium theoretical work links particle stability in polymer nanocomposites to several parameters: the relative polymer segment−particle interaction strength, ε_{pc}; the range of the surface interaction, α; the particle volume fraction, ϕ_c; the particle to polymer segment size ratio, D_c/d; and the polymer degree of polymerization, N.[11−13] Variation of these parameters controls particle miscibility with the theory predicting the conditions of macroscopic phase separation of particles through either depletion-induced phase separation or the formation of a particle−polymer bridged network.[11,12] The crossing of either of these phase boundaries may lie at the origin of mechanical enhancement associated with the presence of particles in polymer matrices. The location of the phase boundaries are most sensitive to changes in ε_{pc} α, and ϕ_c but are also predicted to be susceptible to changes in D_c/d and weakly on N. The potential mechanical consequences of polymer confinement and alteration in polymer relaxations in the presence of particles are not included in the theoretical framework. These effects have been shown to be important in confinement studies of polymer melts using the surface forces apparatus (SFA)[8,9,14−18] and in nuclear magnetic resonance (NMR)[19−23] and quasielastic neutron scattering (QENS)[24] studies of polymer nanocomposites.

In our studies of the origins of nanocomposite mechanical properties, we have worked with a model system composed of hard spheres suspended in a polymer melt. While the particles interact with only volume exclusion interactions, the polymer segments have an affinity for the polymer surface. We have previously studied silica particles dispersed in unentangled polymer melts of poly(ethylene oxide) (PEO).[25,26] Flow properties were found to be well described by models developed for particle suspensions in low molecular weight, Newtonian solvents. Particle pair interactions proved to be hard-sphere-like when the particle's hydrodynamic size was increased to account for adsorbed polymer on the particle surface. The thickness of the adsorbed polymer as measured by hydrodynamic response of the nanocomposite was found to be independent of particle volume fraction and to scale on the polymer radius of gyration, R_g. This behavior results in an effective hydrodynamic volume fraction, ϕ_η, that is larger than the core silica particle volume fraction, ϕ_c. At particle concentrations where $\phi_\eta > 0.56$, the nanocomposites display two well-defined relaxation times with mechanical properties well described by those expected from the formation of a colloidal glass.[26] These observations are in agreement with polymer confinement studies using the surface forces apparatus where the force required to hold flat plates at a fixed separation shows a strong monotonic repulsion that appears as the gap between the surfaces reaches a separation on the order of the polymer size and has a decay length that scales on R_g.[8,9]

*Corresponding author. E-mail: czukoski@illinois.edu.

 Published on Web 10/08/2009

While the rheology of these nanocomposites could be described in light of an adsorbed polymer layer that increased the hydrodynamic size of the particles, the particle microstructure was not consistent with this result. Small-angle X-ray scattering determination of the particle structure factor indicated the presence of an adsorbed layer at low particle volume fractions, while at high volume fractions the particle packing is not consistent with the hydrodynamic size, suggesting differences in the thermodynamic and hydrodynamic particle sizes.

Here we investigate nanocomposite microstructure and rheology as the polymer size is increased through the entanglement molecular weight. Again working with the PEO−silica system, we study nanocomposite rheology with steady-state and oscillatory shear measurements. The state of the dispersion is characterized by using small-angle X-ray scattering (SAXS) to extract particle structure factors. Low volume fraction viscosities and SAXS measurements indicate that polymer adsorption enhances both the thermodynamic and hydrodynamic effective hard sphere particle size. At higher volume fractions, but still below an effective volume fraction where particles are expected to form a colloidal glass, relaxations slow and the viscosity of the nanocomposite diverges. These experiments demonstrate that the effects of polymer entanglement dominate nanocomposite mechanical properties before ϕ_η exceeds the colloidal glass transition. We interpret rheological measurements as resulting from entanglement of adsorbed polymer layers.

As the volume fraction is raised, stress is stored in these entanglements associated with adsorbed polymer resulting in elevation of the low frequency linear viscoelastic moduli in a manner that does not suggest glassy dynamics seen in the unentangled nanocomposites. At the highest volume fractions studied, the nonlinear elastic modulus has two transition yield strains and an intermediate softening regime. In addition, the viscous modulus has two maxima. These phenomena signal a two-step mechanism for the breakdown of structure in the nanocomposite. The yield at low strain is associated with distortion of a particle−polymer network, and the yield at larger strains is associated with disruption of entangled and bridging polymers enabling breakup of the particle−polymer network.

SAXS studies indicate that particle microstructure becomes less sensitive to the degree of polymerization as the polymer weight and nanocomposite volume fraction increase. An unusual fluid to brittle transition is observed at a common volume fraction for PEO molecular weights of 2000 and above. On the basis of scattering measurement of the particle structure factor, this transition is associated with the onset of attractions, suggesting that it is the result of a phase separation.

From these results, we define four critical colloidal volume fractions, ϕ_c. The first occurs when particle surface separations become less than $6R_g$ and bulk polymer entanglement dynamics are altered due to entanglement of free polymer between adsorbed polymer on neighboring particles. This critical entanglement volume fraction, $\phi_{c,e}$, only applies to entangled nanocomposites. A second critical volume fraction, ϕ_c^*, occurs when adsorbed polymer is confined between two neighboring particles. This volume fraction defines overlap of adsorbed polymer layers at a surface separation of $3.6R_g$. A third critical volume fraction, $\phi_{c,g}$, defines when ϕ_η, the effective hydrodynamic particle volume fraction, exceeds the colloidal glass transition volume fraction. This is based on the adsorbed polymer increasing the hydrodynamic particle size by $2.9R_g$ and occurs when the effective particle volume fractions exceeds 0.58. The effective size is determined from the low volume fraction nanocomposite melt viscosity where the particles are treated as hard spheres. Above $\phi_{c,g}$, particles will be confined in effective cages, and the nanocomposite melt will respond mechanically like a glass. For the choices of R_g/D_c in this study, $\phi_c^* > \phi_{c,g}$ when the PEO molecular weight is below 1650 g/mol. Thus, when the molecular weight is below 1650 g/mol, the PEO nanocomposites will form colloidal glasses before the adsorbed polymer is confined while above this molecular weight, polymer entanglement and the stress relaxation mechanisms associated with polymer entanglement and confinement dominate dense composite behavior. Finally, we locate a fluid to brittle transition, $\phi_{c,b}$, in the nanocomposite melts when the polymer molecular weight is greater than 2000 g/mol. This transition occurs at a molecular weight independent particle volume fraction of $\phi_{c,b} = 0.317$ and appears to be insensitive to polymer molecular confinement defined by ϕ_c^* even when ϕ_c^* is less than $\phi_{c,b}$, which occurs for molecular weights greater than 5600 g/mol. Brittleness is associated with a nonlinear mechanical response where the nanocomposite melt fractures as the strain is increased.

Table 1. Polymer Properties

MW	N^a	R_g [nm]	T_m [°C]	$\eta_p{}^b$ [Pa s]
PEO400	9	0.8	8	0.016
PEO1000	23	1.3	40	0.035
PEO2000	45	1.9	53	0.090
PEO8000	182	3.8	63	1.6
PEO20000	455	5.9	65	26

[a] Number of monomers. [b] Temperature of 75 °C.

Below in section II, sample preparation and measurement techniques are described. Results are presented and discussed in section III regarding nanocomposite melt viscosities and viscoelastic properties followed by scattering results and discussion of the nanocomposite melt particle microstructures. Comparisons are made with nanocomposite melts composed of the same particles and polymers with molecular weights below the point of entanglement. A summary of the results and conclusions is presented in section IV.

II. Experimental Methods

A. Sample Preparation. Silica particles were synthesized by the base-catalyzed hydrolysis and condensation of tetraethyl orthosilicate according to the method of Stöber et al.[27] The synthesis produces an alcosol solution of silica particles. Particles were synthesized with a number-average diameter of 43 ± 4 nm as determined from TEM measurements and a volume average diameter of 44 ± 4 nm determined from static scattering measurements. We predict a particle to segment size ratio of 35 based on a Kuhn segment diameter, d, of 1.2 nm ($d = C_\infty l/\cos(\theta/2)$ where $C_\infty = 6.9$ is the experimental characteristic ratio of PEO,[28] $l = 1.5$ Å is the length of a backbone bond, and $\theta = 68°$ is the angle of a backbone bond). Particles were dispersed in PEO ranging in molecular weight from 2000, 8000, and 20 000 purchased from Sigma-Aldrich. Polymer properties are listed in Table 1. The molecular weight of entanglements, M_e, in PEO is 2000, making 8000 and 20 000 modestly entangled polymers. Entanglements begin to affect the rheology of the neat polymer at the critical molecular weight of entanglement, $M_c \approx 2M_e$, of 4000 in PEO determined from the point when the scaling of neat PEO melt viscosity changes from M to $M^{3/2}$. Particle dispersions were made by mixing the alcosol and PEO at a temperature above the melting point of PEO where PEO is miscible in ethanol. The ethanol is evaporated in a vacuum oven purged with nitrogen to avoid PEO degradation.

The method of mixing the alcosol and the PEO is crucial to obtaining well-dispersed particles. Premature particle flocculation occurs if the polymer is diluted too extensively with the addition of alcosol. The time of particle flocculation varies from days to near instantaneous depending on the molecular weight of the polymer. Higher molecular weight polymers flocculate the particles more rapidly. Particle flocculation can be overcome by concentrating the alcosol so that the polymer is diluted less. We believe the polymer initiates depletion flocculation of the particles under dilute polymer conditions. Under concentrated conditions,

the particles restabilize in the polymer solution. The alcosol is gently added to the PEO at a temperature above T_m of the polymer such that the alcosol lies above the PEO. The two layers are rapidly mixed on a vortex stirrer. The resulting mixture is light blue reminiscent of the alcosol before the addition of PEO. Once the ethanol is evaporated, the filled polymer is transparent since PEO and silica have similar refractive indices. The particle volume fraction, ϕ_c, was calculated through eq 1. The nanocomposite density, ρ_T, was measured using a Mettler/KEM DA-100 density/specific gravity meter from the measured density of the nanocomposite. The density of the silica, ρ_c, was previously measured via light scattering to be 1.6 g/mol.[29] Other variables are the mass of silica, m_c, and mass of polymer, m_p.

$$\phi_c = \frac{\rho_T}{\rho_c}\left(\frac{m_c}{m_c + m_p}\right) \tag{1}$$

B. Rheology. Rheological experiments were performed using a constant stress C-VOR Bohlin rheometer with cone−plate and plate−plate geometry. The cone was 20 mm in diameter with an angle of 4°, and the plate was 25 mm in diameter. Measurements were made at a sample temperature of 75 °C. This temperature was chosen because it is above the melting temperature of PEO for all molecular weights. The melting temperature of PEO20000 is 65 °C. Cone−plate geometry was used for measuring dilute samples where the filled polymer behaved as a viscous liquid. Plate−plate geometry was used for measuring concentrated samples where the filled polymer behaved as a viscoelastic solid. When using plate−plate geometry, measurements were made at several gap distances to ensure that slip was not influencing measurements. The viscosity of viscous samples was measured from steady-state down−up stress sweeps. The viscoelastic samples were characterized as prepared from the oven. Cooling of the samples below the melting temperature had no effect on the mechanical properties or the structure of the nanocomposite melts.

C. SAXS. Small-angle X-ray scattering (SAXS) was performed at the 8ID-E XOR beamline located at the Advance Photon Source, Argonne National Laboratory. The instrument has effective pinhole collimation removing the need for slit desmearing. Samples were loaded in custom-made aluminum cells sealed with two kapton polyimide slides. The beam path length was ~1 mm. The cells were secured to a heating block set to a temperature of 75 °C and maintained by a Peltier temperature controller. Scattered photons were collected using an area detector. We have found that long exposure of highly viscous and viscoelastic samples to high-intensity X-rays causes the formation of particle clusters. The clusters of particles are believed to be due to the slowing down of energy dissipation in the illuminated region of the sample as the viscosity of the sample increases. Clustering occurs only in the illuminated region of the sample. This was verified by successive illumination of different regions of the sample. Cluster formation was minimized if the total exposure time to X-rays was limited to less than 60 s.

The scattering intensity of X-rays for a single-component dispersion is given by

$$I(q,\phi_c) = \phi_c V_c \Delta\rho_e{}^2 P(q) S(q,\phi_c) \tag{2}$$

The first term refers to scattering from the particles where ϕ_c is the particle volume fraction, V_c is the volume of a single particle, and $\Delta\rho_e$ is the electron scattering length density of the particles over that of the PEO dispersing phase. The variable q is the scattering vector, $q = (4\pi/\lambda)\sin(\theta/2)$, where λ is the wavelength of incident X-rays and θ is the scattering angle. $P(q)$ is the form factor accounting for intraparticle scattering interference, and $S(q,\phi_c)$ is the structure factor accounting for interparticle scattering interference. Scattering from the silica particles dominates. This enables us to neglect cross-scattering terms between the polymer and particle, and the dispersion is viewed as an effective one-component system.[30−33]

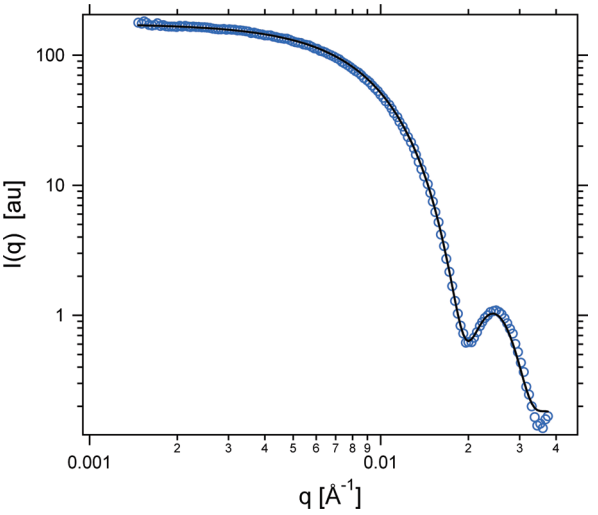

Figure 1. Experimental scattered intensity and model fit [solid line] of a dilute suspension ($\phi_c = 0.01$) of particles in PEO8000 utilizing an average form factor, $\overline{P}(q)$. Fitting parameters are $\overline{D}_c = 44$ nm and $\nu = 4$ nm.

In the dilute particle limit, the structure factor goes to unity and the scattering equation reduces to $I(q,\phi_c) = \phi_c V_c \Delta\rho_e{}^2 P(q)$. The form factor for spherical particles is given by

$$P(q) = \left(3\frac{\sin(qD_c/2) - (qD_c/2)\cos(qD_c/2)}{(qD_c/2)^3}\right)^2 \tag{3}$$

We account for modest polydispersity in particle size by calculating $P(q)$ for a size distribution. This is done by employing a Gaussian diameter distribution to calculate an average form factor for a population of particles with volume average diameter $\overline{D}_c$ and standard deviation ν. The integration variable D_c is the variable diameter of a particle.

$$\overline{P}(q) = \frac{\int \frac{1}{\sqrt{2\pi\nu^2}} e^{-(D_c-\overline{D}_c)^2/2\nu^2} D_c{}^6 P(q)\, dD_c}{\int \frac{1}{\sqrt{2\pi\nu^2}} e^{-(D_c-\overline{D}_c)^2/2\nu^2} D_c{}^6\, dD_c} \tag{4}$$

Experimental scattering of dilute nanocomposites are fit to the scattering equation utilizing eq 4 for the form factor to determine a scattering size and standard deviation in the polymer melt (Figure 1). The fitting procedure has three adjustable parameters: particle diameter, standard deviation, and electron contrast density.

As the volume fraction of filler is raised, the structure factor measures the spatial distribution of filler particles in inverse space. Formally, the structure factor for a single-component dispersion is defined as the Fourier transform of the nonrandom part of the pair correlation function, $g_{cc}(r)$.

$$S(q,\phi_c) = 1 + \frac{\phi_c}{V_c}\int_0^\infty 4\pi r^2 [1 - g_{cc}(r)]\frac{\sin(qr)}{qr}\, dr \tag{5}$$

The term $[1 - g_{cc}(r)]$ is often called the total correlation function, $h_{cc}(r)$. In order to determine the real space distribution of particles, one must take the inverse Fourier transform of $S(q,\phi_c)$ to find $g_{cc}(r)$.

Experimental structure factors for concentrated nanocomposites are calculated by dividing the intensity of a concentrated nanocomposite by the intensity of a dilute nanocomposite (dil),

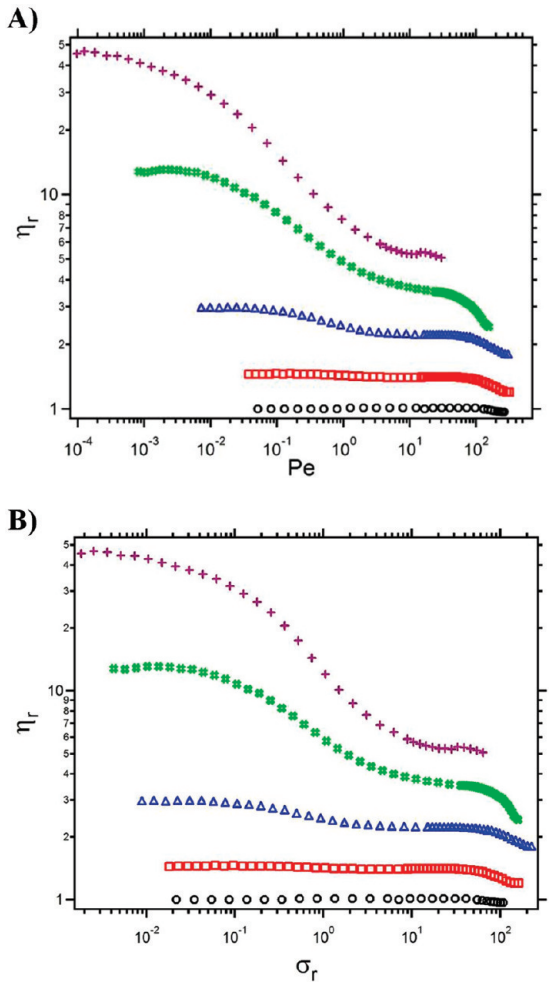

Figure 2. Measurement of the relative viscosity of PEO8000 nanocomposites versus (A) *Pe* and (B) σ_r for ϕ_c of 0.000 [○], 0.058 [□], 0.128 [△], 0.192 [#], and 0.234 [+].

eq 6. In the dilute limit, the structure factor goes to unity since particle positions are uncorrelated. The result leaves $S(q,\phi_c)$ for the concentrated nanocomposite

$$S(q,\phi_c) = \frac{I(q,\phi_c)}{I_{dil}(q,\phi_c)}\frac{\phi_{c,dil}}{\phi_c} \tag{6}$$

III. Results and Discussion

A. Nanocomposite Rheology. The steady shear viscosity of a nanocomposite melt composed of silica particles suspended at several volume fractions in PEO8000 is shown as a function of the dimensionless shear rate, the Peclet number, *Pe*, and the reduced stress, σ_r, in Figure 2. We define the Peclet number as $Pe = 3\pi\eta_p\dot{\gamma}D_c^3/4k_BT$, where η_p is the neat melt viscosity, $\dot{\gamma}$ is the shear rate, and k_BT is the product of Boltzmann's constant and absolute temperature. The reduced stress is defined as $\sigma_r = \sigma D_c^3/k_BT$ where σ is the applied shear stress. In the absence of particles, the polymer shear thins near $Pe = 10^2$. Shear thinning occurs as the shear rate exceeds the rate of polymer relaxation.[34] The critical shear rate for the onset of shear thinning is inversely proportional to longest polymer relaxation time, $\dot{\gamma}_c \sim \tau_1^{-1}$.[34,35] Polymer molecular relaxation is made up of a spectrum of relaxation times. In entangled polymers, shear thinning is influenced by the time scale for the renewal of entanglements. A high shear plateau is reached when the shear rate is greater than the rate of all polymer relaxations. It is difficult to reach the high shear plateau due to secondary flows.

At low ϕ_c, the flow behavior mimics that of the neat polymer with a low shear rate plateau viscosity that increases with particle volume fraction. As ϕ_c increases, the nanocomposite melts show two shear thinning regimes. The first shear thinning regime is absent in the neat polymer and is attributed to the relieving of thermodynamic stresses stored in the particle microstructure due to Brownian forces acting on the particles. As the shear rate is increased, Brownian forces are less important, leaving only a particle hydrodynamic contribution to the viscosity.

At high shear rates, the second shear thinning regime is associated with shear thinning of the polymer. (The second shear thinning regime became more difficult to measure as ϕ_c increased due to loss of sample from underneath the cone at high shear rates.) The onset of the second shear thinning regime occurs at progressively lower *Pe* as ϕ_c is increased, but the onset to shear thinning occurs at a constant reduced stress of $\sigma_r \approx 40$. The nanocomposite melts appear to shear thin more than the neat polymer, but it is difficult to gauge the magnitude of the drop in viscosity at the second shear thinning limit because secondary flows hinder measurement of the viscosity at high shear rates. It is also not immediately apparent whether the shear thinning in the nanocomposite melt is the same as the neat melt or whether other events are contributing to thinning. The constant stress onset of thinning suggests that the mechanism of thinning is similar between the nanocomposites and the neat melt. Thinning of the neat melt is initiated when the shear rate exceeds the longest time scale for the renewal of entanglements. The greater thinning of the nanocomposite melts may show that the particles are enabling more stress to be stored in the polymer matrix, specifically entanglements, since thinning in the polymer melt is related to shearing entanglements. The higher the particle concentration, the greater the amount of stress stored in the polymer matrix. Shearing of the nanocomposite is shown to relieve these stresses. Of interest is answering the question of how the particles enable stress to be stored in the polymer matrix.

Low Volume Fraction Viscosity and Evidence for Entanglement at the Pair Level. As a starting point to understanding the rheological enhancement due to particles in an entangled polymer melt, we begin by discussing the effect of increasing ϕ_c on the low shear rate, low volume fraction viscosity. We assume that the nanocomposites may be viewed as a suspension of particles in a high-viscosity continuum of polymer segments. Under this premise, the low shear relative viscosity, $\eta_{r,0} = \lim_{Pe\to 0}\eta/\eta_p$, of the filled polymer melts at low volume fractions may be written as

$$\eta_{r,0} = 1 + [\eta]\phi_c + P\phi_c^2 \tag{7}$$

where η is the viscosity of the nanocomposite and η_p is the viscosity of the neat polymer, $[\eta]$ is the particle intrinsic viscosity, and *P* is the pair interaction coefficient that defines the contribution of two particle interactions to the viscosity. Since the particles are spherical, we define the intrinsic viscosity as $[2.5k]$ where 2.5 is Einstein's coefficient and *k* is a parameter that defines how the adsorption of polymer segments influences the particle intrinsic viscosity. Equation 7 is linearized in terms of the volume fraction to the reduced viscosity, η_{red},

$$\eta_{red} = \frac{\eta_{r,0}-1}{\phi_c} = [\eta] + P\phi_c \tag{8}$$

In Figure 3, the reduced viscosity is plotted as a function of ϕ_c, and the data are fit to eq 8. Results for parameters

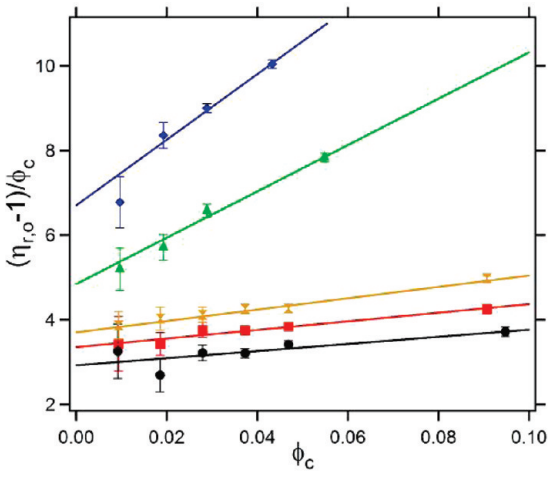

Figure 3. Measurement of the low shear reduced viscosity of PEO400 [●], PEO1000 [■], PEO2000 [solid ⧖], PEO8000 [▲], and PEO20000 [♦]. Solid lines show linear fits to eq 8.

Table 2. Viscosity Coefficients

MW	k	P	P/k^2
PEO400	1.18 ± 0.04	8.4 ± 1.8	6.0 ± 1.3
PEO1000	1.34 ± 0.05	10.1 ± 1.3	5.6 ± 0.7
PEO2000	1.48 ± 0.03	13.4 ± 1.1	6.1 ± 0.5
PEO8000	1.94 ± 0.09	55 ± 9	14.5 ± 2.5
PEO20000	2.69 ± 0.14	77 ± 17	10.7 ± 2.4

k and P are reported in Table 2. Results for PEO400 and PEO1000 were reported previously and are shown here again for comparison with the entangled nanocomposites.[25] In Table 2, k is shown to increase with molecular weight meaning that the particle intrinsic viscosity is increasing as the molecular weight is raised.

In agreement with studies of polymer melts confined between two surfaces,[8,14−16,18,36] this result suggests that attractions between polymer segments and the surface result in an increase in the particle's hydrodynamic size due to the formation of an adsorbed polymer layer that scales on the polymer radius of gyration, R_g. This approach allows k to be interpreted as an enhanced particle volume such that $k = \phi_\eta/\phi_c$, where ϕ_η defines an effective volume fraction due to the larger particle hydrodynamic size. A linear relationship between $k^{1/3}$ and R_g/D_c in Figure 4 clearly shows that k increases as $k = [1 + (2.82 \pm 0.08)R_g/D_c]^3$. This linear relationship holds as the polymer molecular weight passes through M_c which occurs at $R_g/D_c = 0.060$. Figure 4 supports our conclusion that the single particle contribution to the nanocomposite viscosity is well described as arising from particles with a hydrodynamic size increased over the bare particle due to the formation of an adsorbed layer with a thickness that scales on R_g.

Within experimental uncertainty, P/k^2 in the unentangled nanocomposite melts agrees well (Table 2) with the model hard sphere value of 5.9.[37] However, in the entangled nanocomposite melts P/k^2 is larger than the value expected for hard spheres. This suggests that, in addition to an adsorbed polymer layer that increases a single particle's contribution to the nanocomposite viscosity, there are additional contributions to pair interactions above and beyond volume exclusion and a no slip boundary condition in a viscous continuum.

Dense Nanocomposite Viscosity. The effect of the stronger contribution is evident at higher volume fractions when the low shear viscosity is plotted versus ϕ_η in Figure 5 where

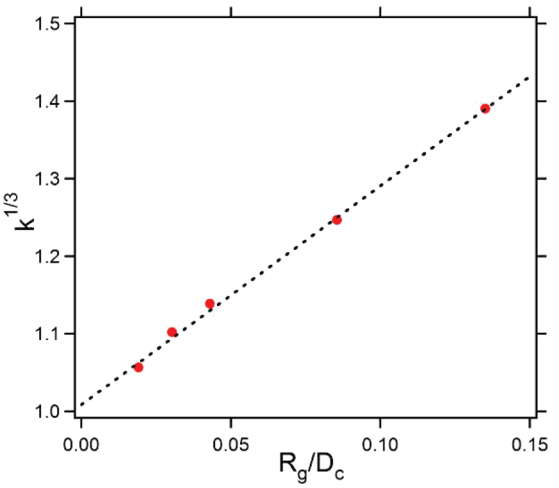

Figure 4. $k^{1/3}$ is plotted as a function of R_g/D_c for 44 nm diameter particles. The data are linear and verify scaling of the thickness of an adsorbed polymer shell around the particles on polymer R_g. The dashed line is a linear fit to the data and has a slope of 2.82 ± 0.08.

$\phi_\eta = (1 + 2.82R_g/D_c)^3\phi_c$. As shown previously, using ϕ_η as a measure of particle volume fraction, the low shear rate viscosities of the unentangled nanocomposite melts collapse onto a single curve that closely follows that expected of hard spheres suspended in a Newtonian continuous phase.[25] However, in the entangled nanocomposite melts, the viscosity rises above that expected for hard spheres with effective sizes of $D_\eta = D_c(1 + 2.82R_g/D_c)$, indicating that both pair and higher order interactions appear larger than expected of hard spheres of size D_η.

Surface force measurements of polymer melts confined between plates provide insight into the stronger contribution of particle pair interactions in entangled nanocomposites.[8,9,15] Israelachvili and Kott report that the force profile of a low molecular weight unentangled polymer melt resembles a hard-wall-like repulsion when the plates are separated by a distance of $\sim 2-3R_g$.[15] When the polymer molecular weight is increased to M_c, a weak repulsive tail is added onto the strong hard-wall repulsion near the surface. When confining the higher molecular weight polymer to a gap of $< 3R_g$, an attractive well appeared as the surfaces were pulled apart at a surface separation where, when driving the surfaces together, a repulsive interaction was observed. Other studies of confined polymer melts demonstrate that when surfaces are separated at a distance where the repulsion is not experienced, the polymer retains its bulk viscosity with a no slip boundary condition offset $\sim 2R_g$ from the surface.[8,9] However, at surface separations where the polymer is confined sufficiently to produce a repulsion, the polymer viscosity is larger than the bulk. These studies suggest particle interactions in entangled polymers are softer, and when particle separations become smaller than the range of the repulsion, the nanocomposite melt viscosity will be affected by both the volume fraction of particles and confinement of the polymer.

In our nanocomposites, the average separation where polymers between the particles behave in a manner that is not consistent with bulk behavior occurs at $\sim 3.6R_g$. This measure of the onset of polymer confinement was observed previously for unentangled PEO nanocomposites.[38] We use this surface separation to define the onset of polymer confinement in entangled nanocomposites and define the volume fraction where this occurs as $\phi_c^* = 0.63/(1 + 3.6R_g/D_c)^3$.

Linear Viscoelasticity: Particle Glasses and Entangled Polymer Dynamics. As ϕ_c approaches $\phi_{c,g}$ in unentangled

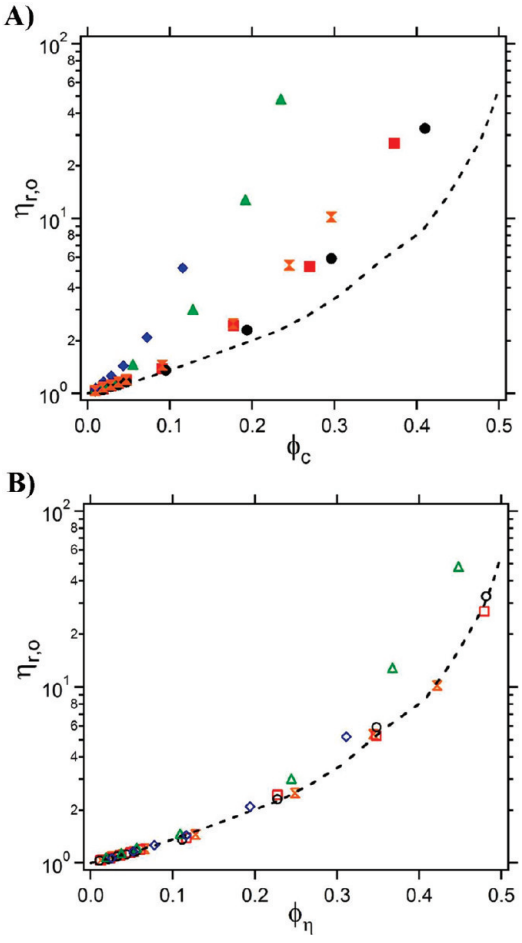

Figure 5. Low shear viscosity of PEO400 [●, ○], PEO1000 [■, □], PEO2000 [solid ⧖, ⧖], PEO8000 [▲, △], and PEO20000 [♦, ◊] plotted versus (A) ϕ_c and (B) ϕ_η. The dashed line represents reported experimental hard sphere data.[53]

PEO nanocomposites, slowly relaxing glassy particle domains percolate at short time and relax at longer time. As ϕ_c increases through $\phi_{c,g}$, long-range self-diffusion is essentially eliminated if the polymer hydrodynamic size remains fixed. For large particles and low molecular weights, $\phi_{c,g} < \phi_c^*$. Therefore, particles form a colloidal glass before confinement effects of the polymer contribute to the viscosity of the nanocomposite melt. As the polymer molecular weight is increased or the particle diameter is decreased, ϕ_c^* will eventually become lower than $\phi_{c,g}$ such that the effects of polymer confinement will occur before the formation of a colloidal glass. For the 44 nm diameter particles studied here this occurs when $R_g/D_c = 0.039$.

For $R_g/D_c < 0.039$, the particles will form a colloidal glass before the polymer experiences confinement. Under this condition and when $\phi_c > \phi_{c,g}$, stress is stored in cage deformation of the repulsive particle glass. Only when $\phi_c > \phi_c^*$ will there be a contribution from the confined polymer. When $R_g/D_c > 0.039$, polymer confinement effects will impact the nanocomposite mechanical behavior prior to a colloidal glass transition. In fact, when $R_g/D_c > 0.039$, the idea of a colloidal glass transition is questionable. Further addition of particles, which removes polymer from the nanocomposite, will affect the thickness of the adsorbed polymer layer. Values of ϕ_c^* and $\phi_{c,g}$ are given in Table 3.

In Figure 6, we present the linear viscoelastic moduli as a function of strain frequency for PEO400 nanocomposites where $R_g/D_c < 0.039$ and PEO20000 nanocomposites where

Table 3. ϕ_c^* and $\phi_{c,g}$ of Particles in PEO

MW	$\phi_{c,g}$	ϕ_c^*
400	0.496	0.516
1000	0.455	0.462
2000	0.413	0.410
8000	0.305	0.282
20000	0.222	0.192

$R_g/D_c > 0.039$. The moduli are nondimensionalized by the effective particle hydrodynamic diameter and the thermal energy, and the frequency is nondimensionalized by the effective particle hydrodynamic diameter and the dilute particle diffusion coefficient, $D_0 = k_BT/3\pi\eta_pD_\eta$. Moduli and frequency were nondimensionalized by the effective particle hydrodynamic diameter since this measure of particle size was determined from dilute viscosity measurements. ϕ_η and a_{cc}, the average particle surface separation in terms of R_g, are listed in Table 4 for the data presented in Figure 6. The average surface separation scaled on the polymer radius of gyration is calculated using the formula $a_{cc} = (D_c/R_g)$-$[0.63/\phi_c)^{1/3} - 1]$.

When comparing the two sets of data, the first major difference lies in the measurable dimensionless frequency window. The dimensionless frequency is controlled by the viscosity of the polymer and size of the particles and sets the time scales over which particle dynamics can be monitored. Because of a low neat melt viscosity of PEO400, we are able to probe more than 3 orders of magnitude lower in dimensionless frequency than the PEO20000 emphasizing that, at the same ϕ_η, particle relaxations in the entangled nanocomposite take at least 3 orders of magnitude longer than in the unentangled nanocomposite.

The frequency dependence of the moduli of the PEO400 and PEO20000 nanocomposites are dramatically different. The PEO400 nanocomposites show signs of a classical colloidal glass transition. A plateau in the elastic modulus emerges at high frequency and grows in magnitude as ϕ_c approaches and exceeds the glass transition volume fraction, $\phi_{c,g} = 0.496$. The terminal flow regime shifts to lower frequency. Over the frequency range of the plateau in the elastic modulus, a minimum and a maximum develop in the viscous modulus that shift to lower frequencies as the volume fraction is increased. These frequencies characterize β (minimum) and α (maximum) relaxations in the particle glass and were previously shown to have power law scaling as a function of volume fraction in the unentangled nanocomposite, in agreement with other glass-forming systems.[38]

In PEO20000 nanocomposites, $R_g/D_c > 0.039$, leading to the expectation that polymer confinement effects will preempt a colloidal glass transition. The neat polymer is dominated by viscous behavior, yet an elastic contribution is measurable. Terminal flow behavior is seen at low frequency. Between dimensionless frequencies of 10 and 0.1, the elastic modulus has a slope of 0.5. At high frequencies, the elastic modulus scales as ω^2, resembling terminal flow. The entanglement plateau of PEO occurs at much higher frequencies beyond the measurement window, and the entanglement modulus is much higher than can be measured (1.8 MPa).[4,39] The origin of the change in the scaling of the elastic modulus between dimensionless frequencies of 10 and 0.1 is not known.

As particles are introduced into the polymer, the moduli for $\phi_c = 0.052$ are shifted up but qualitatively do not change, suggesting the rheology is well described by the physical picture of particles dispersed in a viscous continuum when the particle volume fraction can be considered dilute. The effective particle size is increased due to adsorbed polymer, but outside of the adsorbed layer, the polymer appears to

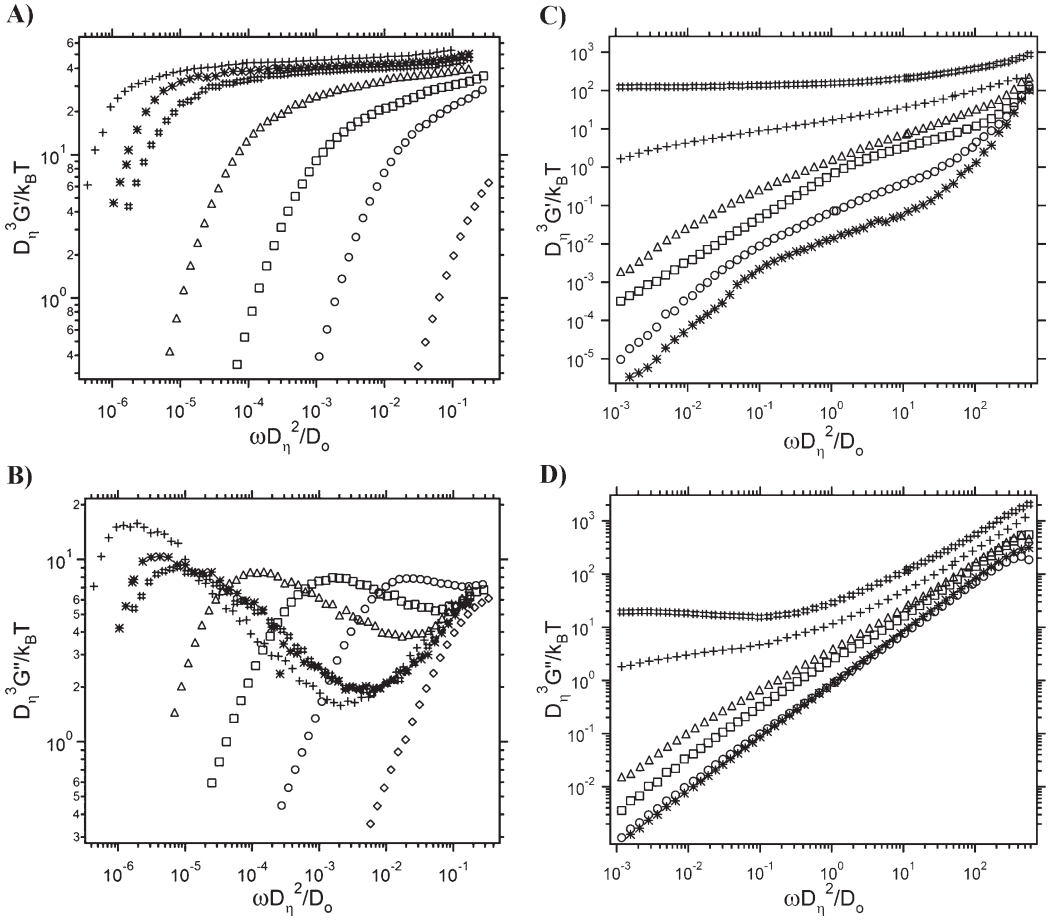

Figure 6. (A, B) PEO400 linear dimensionless elastic and viscous moduli versus frequency at ϕ_c of 0.455 [◇], 0.484 [○], 0.489 [□], 0.494 [Δ], 0.499 [#], 0.504 [∗], and 0.509 [+]. (C, D) PEO20000 linear elastic and viscous moduli versus frequency at ϕ_c of 0.000 [∗], 0.052 [○], 0.135 [□], 0.173 [Δ], 0.214 [+], and 0.265 [#].

Table 4. Effective Volume Fraction and Particle Surface Separation in PEO400 and PEO20000[a]

PEO400			PEO20000		
ϕ_c	ϕ_η	a_{cc}	ϕ_c	ϕ_η	a_{cc}
0.455	0.535	6.0	0.052	0.140	9.6
0.484	0.569	4.8	0.135	0.364	5.0
0.489	0.575	4.6	0.173	0.466	4.0
0.494	0.581	4.4	0.214	0.577	3.2
0.499	0.587	4.2	0.265	0.714	2.5
0.504	0.592	4.0			
0.509	0.598	3.9			

[a] a_{cc} is the average particle surface separation in terms of R_g.

retain its bulk viscoelastic properties within the measured frequency window. Polymer relaxations taking place in the adsorbed layer must lie at lower frequencies (longer time) outside of the measurement window.

At $\phi_c = 0.135$ where $a_{cc} < 6$, the elastic and viscous moduli are further elevated and the low-frequency behavior is changed, suggesting an increase in the length of the terminal relaxation time of the nanocomposite over that of the neat polymer. The volume fraction is less than $\phi_c^* = 0.192$. As a result, we do not anticipate that polymer confinement will substantially influence the longest relaxation time in the nanocomposite. Instead, the qualitative change in behavior is partially due to continued reduction in the diffusion rate of the particles due to the elevated particle volume fraction. In addition, at $\phi_c = 0.135$ in Figure 5, the low shear rate viscosity is larger than expected for hard spheres of diameter D_η. This increase (above what is seen in unentangled polymer melts) suggests that entanglements are influencing nanocomposite melt dynamics. One interpretation of these observations is to attribute the change to secondary entanglements defined as entanglements between nonadsorbed polymer and adsorbed polymer on two neighboring particles.[1] Relaxation of secondary entanglements will be slower than bulk entanglements since dynamics of the adsorbed chain is slowed due to proximity to the surface and would appear at lower frequency than bulk entanglements.

For PEO20000, above $\phi_c = 0.173$, ϕ_c approaches and exceeds ϕ_c^*, causing an elevation in moduli and an extension of the terminal regime to lower frequency. For $\phi_c \geq 0.214$, the polymer is held to a layer thickness where we expect confinement effects to become important. In the PEO20000 samples, we do not see the glassy dynamics seen in PEO400 at a similar ϕ_η. For $\phi_c > \phi_c^*$, the adsorbed layers are likely to interpenetrate. Under these conditions, our results suggest the impact of confining the polymer preempts the glass transition.

Onset of Nonlinear Viscoelastic Response: Entanglement-Induced Secondary Yielding. The buildup of elasticity in the entangled nanocomposite is further studied by oscillatory stress sweeps which show how the emerging new structure responds to a growing external stress. In Figure 7, we show the strain dependence of the moduli for PEO 400, 8000, and 20000 nanocomposites. In Table 5, ϕ_η and a_{cc} are listed for the data shown in Figure 7. In both cases we note that the range of volume fractions studied passes through $\phi_{c,g}$ (0.496 for PEO400, 0.305 for PEO8000, and 0.222 for PEO20000). The response of the nanocomposite to an applied stress is

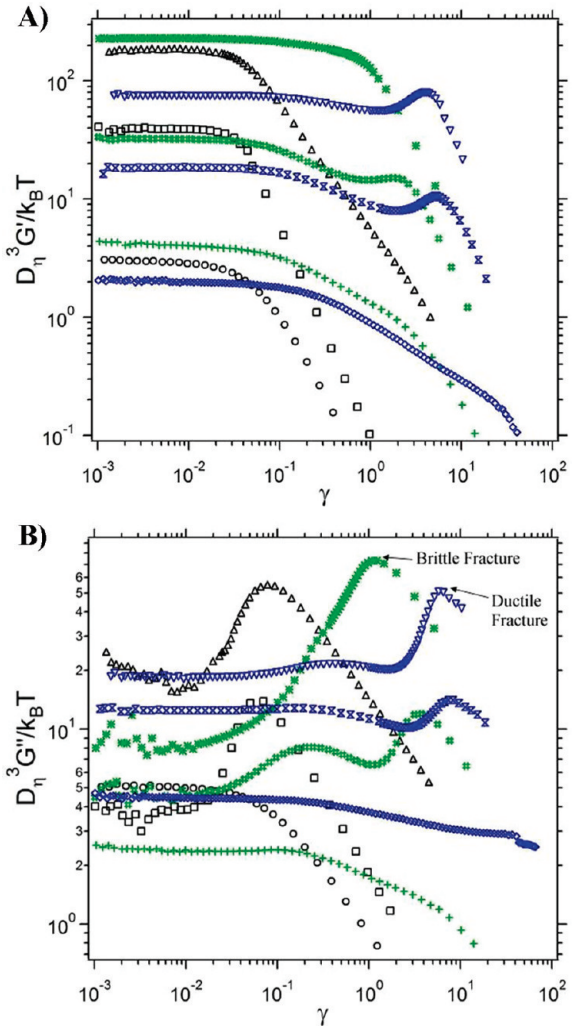

Figure 7. Dimensionless (A) G' and (B) G'' as a function of strain at a frequency of 0.1 Hz for PEO400 at ϕ_c of 0.489 [○], 0.504 [□], and 0.524 [△], PEO8000 at ϕ_c of 0.255 [+], 0.296 [#], and 0.317 [∗], and PEO20000 at ϕ_c of 0.173 [◇], 0.204 [⧖], and 0.265 [▽].

linear at low strain and nonlinear at high strain. At low strain, local thermal fluctuations can relax the applied stress without destruction of the structure. At high strain, the structure is broken down. Insight is gained into the mechanism for structure degradation through studies of how the moduli change between these extremes in behavior.

The unentangled and entangled nanocomposites have different strain behavior. PEO400 illustrates the strain softening of a mechanically weak particle glass. The effective volume fractions are in the range where we expect to see glassy behavior (Table 3). Over a volume fraction range of $0.489 < \phi_c < 0.524$, the average interparticle separation changes from $4.6R_g$ to $3.3R_g$ such that the polymer is confined only at the highest volume fraction. In this system, there is no evidence of particle attractions even when the polymer is confined. Yielding of the confined PEO400 nanocomposite is similar to the unconfined PEO400 nanocomposite, but the viscous modulus is dramatically increased, showing that confinement of PEO400 has increased the polymer viscosity but the yielding behavior is the same. The elastic modulus reaches 0.9 of its low strain value at a strain of ~0.03 for all volume fractions. At this strain, the particle cages are sufficiently distorted that thermal fluctuations allow particles to rearrange. A decrease in the elastic modulus is accompanied by the viscous modulus increasing and passing through a maximum. The maximum is associated with a transition from solid to liquid-like behavior and can be attributed to stress-accelerated breakup of percolated glassy domains required to allow the unentangled nanocomposite to flow.

Table 5. Average Interparticle Separation Distance, a_{cc}, in Terms of Polymer R_g and the Effective Particle Volume Fraction, ϕ_η, for Data Shown in Figure 7

PEO400			PEO8000			PEO20000		
ϕ_c	ϕ_η	a_{cc}	ϕ_c	ϕ_η	a_{cc}	ϕ_c	ϕ_η	a_{cc}
0.489	0.572	4.6	0.255	0.495	4.1	0.173	0.466	4.0
0.504	0.590	4.0	0.296	0.575	3.3	0.204	0.550	3.4
0.524	0.613	3.3	0.317	0.616	3.0	0.265	0.714	2.5

PEO8000 and PEO20000 nanocomposite melts do not show the glass-like yielding mechanism of PEO400. The entangled nanocomposites have an intermediate strain softening regime with the exception of the highest volume fraction in PEO8000. At the lowest volume fractions in the entangled nanocomposites, the average values of a_{cc} are similar. However, the strain at the initial yielding point increases with polymer molecular weight. The intermediate softening regime separates the linear viscoelastic regime from the terminal regime. A second yield strain, seen only for the entangled polymers, is defined by the change in the power law behavior of the elastic modulus and marks the transition to terminal behavior. This second yield strain is present before the polymer is confined, $a_{cc} > 3.6$, and shifts to higher strain with polymer molecular weight. The two yield strains seen in the strain dependence in G' are accompanied by two maxima in the viscous modulus. The appearance of the second maximum indicates the onset of the second relaxation mechanism.

In PEO8000 nanocomposites the second yield appears as the surface separation is reduced from $5.7R_g$ at $\phi_c = 0.192$ to $5.1R_g$ at $\phi_c = 0.214$. This result is shown in Figure 8, and surface separations are listed in Table 6. The two yield points appear when surface separations are roughly $2R_g$ greater than the confined state. This suggests that the appearance of two yield strains is a result of secondary entanglements. This description of the origin of the two yield strains is in agreement with the linear moduli of PEO20000 where the entanglement plateau in the elastic modulus was altered as the surface separation became less than $\sim 6R_g$, and from these observations we then define the third critical volume fraction, $\phi_{c,e} = 0.63/(1 + 5.4R_g/D_c)^3$, characterizing the volume fraction where entanglement dynamics deviate from those seen in the bulk. In PEO8000 and PEO20000, $\phi_{c,e}$ is 0.202 and 0.122, respectively. The onset of two yield points and thus the existence of this secondary entanglement volume fraction is unique to the entangled nanocomposites. There is no observable rheological consequence to $a_{cc} < 5.4$ in unentangled PEO400 and PEO1000 nanocomposites.[38] We thus anticipate $\phi_{c,e}$ to become important in nanocomposite melts only when the molecular weight is greater than M_c.

As ϕ_c is increased in Figure 7, while maintaining a similar particle separation distance in terms of R_g for the two entangled nanocomposites, the first yield strain is relatively unchanged. The value of this yield strain is similar to that seen in many stable, strongly interacting colloidal systems and is associated with shear-induced release of thermodynamic stresses stored in the particle microstructure.[40]

When $\phi_c > \phi_c^*$, the two nanocomposites strain harden at the second yield strain; i.e., G' shows a maximum as strain increases. The degree of hardening is defined by the ratio of G' at the apex of hardening to the minimum in G' at the end of the first softening regime. At the same value of a_{cc}, the strain

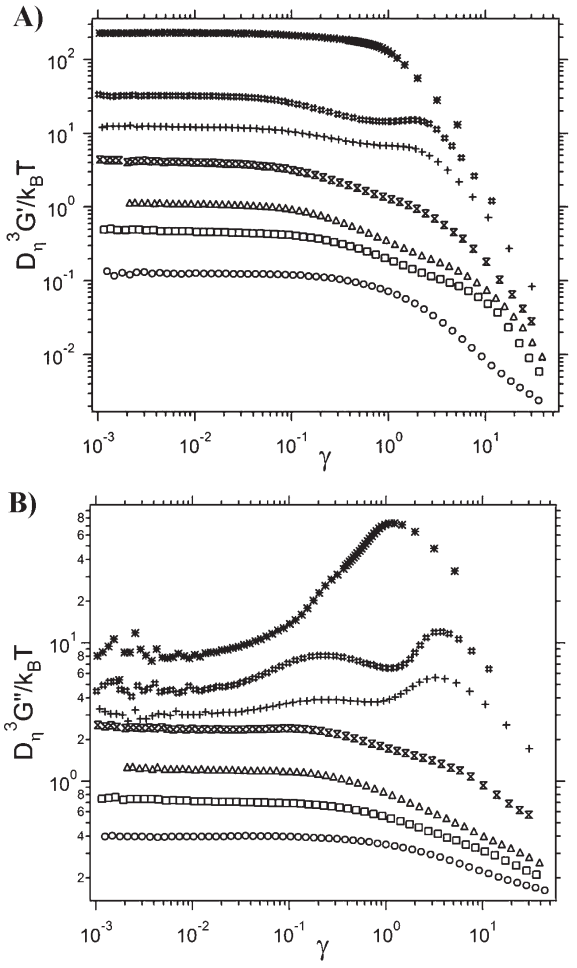

Figure 8. Dimensionless (A) G' and (B) G'' as a function of strain at a frequency of 0.1 Hz for PEO8000 at ϕ_c of 0.192 [○], 0.214 [□], 0.234 [△], 0.255 [X], 0.276 [+], 0.296 [#], and 0.317 [∗].

Table 6. Effective Volume Fraction and Particle Surface Separation in PEO8000

ϕ_c	ϕ_η	a_{cc}
0.192	0.367	5.7
0.214	0.409	5.1
0.234	0.448	4.6
0.255	0.487	4.1
0.276	0.526	3.7
0.296	0.566	3.3
0.317	0.605	3.0

hardening ratio increases with molecular weight from 1.05 in PEO8000 to 1.32 in PEO20000. The appearance of strain hardening as the polymer molecular weight is increased, and the dependence of the relative amount of hardening on molecular weight suggests that hardening is a property of the polymer and linked to confined entanglements. Confinement is associated with surface separations becoming comparable to the thickness of the adsorbed polymer layer on two neighboring particles. In the entangled nanocomposite, we anticipate the rheology of the confined entangled polymer to be determined by entanglements of polymer chains adsorbed on neighboring particles.

Stress sweeps at other frequencies show that the strain of the second yield does not change with frequency, but the degree of strain hardening grows with strain frequency with a greater amount of hardening at higher frequencies (Figure 9A). When plotting the strain hardening ratio as a function of frequency, the

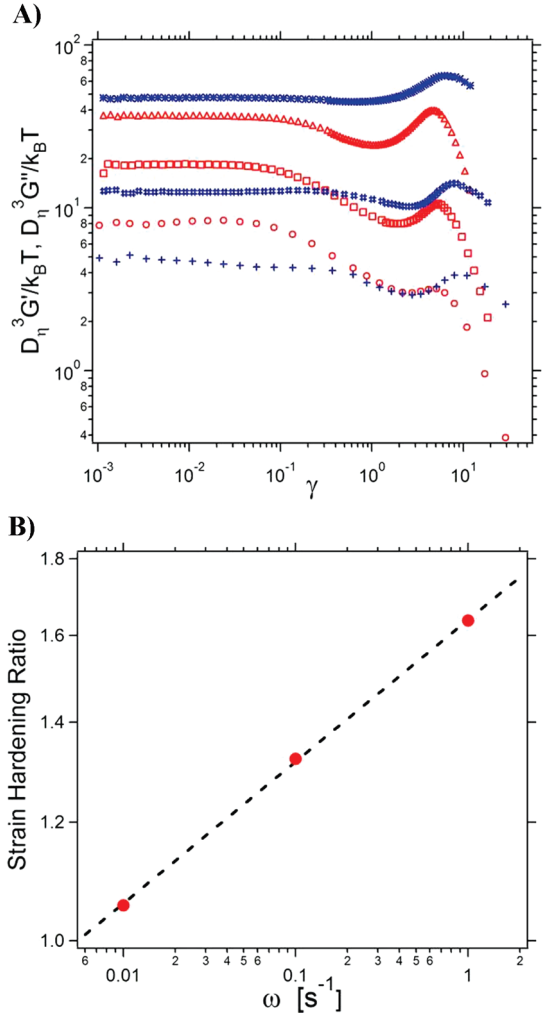

Figure 9. (A) Dimensionless G' and G'' as a function of strain for ϕ_c = 0.204 in PEO20000 at frequencies of 0.01 Hz [○, +], 0.1 Hz [□, #], and 1 Hz [△, ∗]. (B) Strain hardening ratio defined as the ratio of G' at the apex of hardening to G' at the end of the intermediate softening for the stress sweep data in (A) versus the frequency of the oscillations. The dashed line is a fit to a power law with coefficient 1.639 ± 0.006 and exponent 0.095 ± 0.002.

data are well fit by a power law, $G'_{max}/G'_{min} = A\omega^x$, with A = 1.64 ± 0.01 and x = 0.095 ± 0.002 (Figure 9B). At sufficiently low frequencies, the entanglements will relax such that strain hardening will no longer be observed. For this sample, this occurs at a frequency of 5.45×10^{-3} Hz. For lower frequencies, we expect $G'_{max}/G'_{min} = 1$. In polymer matrices, strain hardening originates from the ordering of segments between entanglements. This ordering is entropically unfavorable, thus resulting in an increase in the modulus.[41,42] At higher strains, the ordering is disrupted and terminal flow is then observed producing a maximum in G'.

On the basis of this interpretation, the observed strain hardening can be linked to primary entanglements whose release is restricted due to confinement. If the effective strain rate ($\omega\gamma$) is faster than the time scale for primary entanglements to relax the stress, the entanglements act as physical constraints. When the effective strain rate is slower than the time scale for the release of confined primary entanglements, the stress is dissipated by the continuous release of entanglements. While the frequency dependence of the ratio of G'_{max}/G'_{min} may be the same, we do not expect A and x to apply at other volume fractions since the relaxation time of the polymer is likely to depend on the degree of confinement.

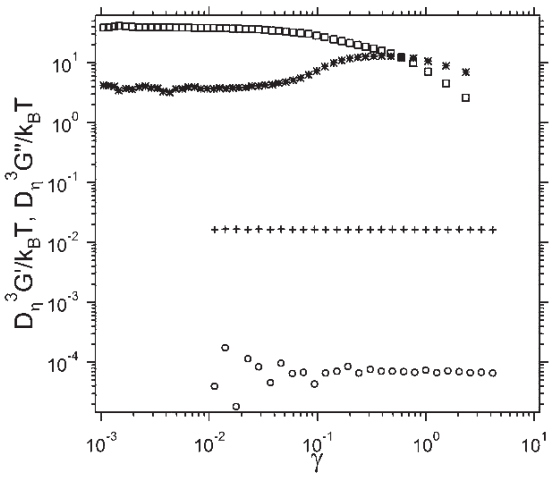

Figure 10. Dimensionless G' and G'' as a function of strain for PEO2000 nanocomposites at $\phi_c = 0.296$ [○, +] and $\phi_c = 0.317$ [□, ∗] at 0.1 Hz.

After hardening, the nanocomposite yields and demonstrates terminal flow behavior. The transition to terminal flow in the elastic modulus is accompanied by a maximum peak in the viscous modulus. The second peak is thus associated with the stress-accelerated release of confined primary entanglements.

Brittle Fracture. In the two most concentrated entangled nanocomposites, the yielding behavior deviates for that seen at lower volume fractions. PEO20000 has the same softening and hardening trends seen at lower ϕ_c. However at high strains, the nanocomposite undergoes ductile deformation and eventually fractures. At lower ϕ_c, the nanocomposites in PEO20000 do not show macroscopic fracture. In contrast, at $\phi_c = 0.317$ the PEO8000 nanocomposite is brittle. The nanocomposite slightly softens at low strain and fractures as the strain approaches unity. The transition from ductile to brittle occurs over a narrow volume fraction range between $\phi_c = 0.296$ and 0.317. Remarkably, PEO2000 nanocomposites also show a brittle transition at $\phi_c = 0.317$. The PEO2000 nanocomposite is a liquid prior to the transition (Figure 10). In the next section, we show that the ductile to brittle transition in PEO8000 and the liquid to brittle transition in PEO2000 are linked to signs of particle phase separation in the melt.

The onset of brittle behavior does not appear to be related to polymer molecular confinement. The surface separation in PEO2000 at $\phi_c = 0.317$ is $6R_g$. In PEO8000 and PEO20000 at surface separations of $6R_g$, a low shear plateau viscosity can be measured. In addition, a PEO20000 nanocomposite at $\phi_c = 0.265$ still displays ductile deformation. This nanocomposite, where the surface separation is $2.5R_g$, continues to show a distinct intermediate softening regime followed by strain hardening and ductile fracture at a strain of 10. At these volume fractions, the particle separation distance is less than $2.8R_g$ (particles are still well dispersed, see Figure 11). Since the particle separation distance is less than $2.8R_g$, we anticipate that polymer dynamics will be heavily influenced by proximity of particle surfaces. (In passing, we note that the overlap of surface adsorbed polymer should not be confused with overlap of grafted polymer layers whose thickness is characterized by $2.8R_g$. The layers are not grafted but are adsorbed. When the particle separation becomes less than $2.8R_g$, the polymer that formed the adsorbed layer at larger surface separations is stripped and most of the remaining polymer conforms to the confined space. Therefore, the calculated ϕ_η in PEO20000 at $\phi_c = 0.265$ no longer describes the effective particle volume fraction.)

B. Particle Microstructure. Particle structure factors are shown in Figure 11 at several volume fractions in PEO2000, PEO8000, and PEO20000. At first glance, there is striking similarity between the particle structure in PEO8000 and PEO20000. In PEO2000, the particles are less structured than in the two higher molecular weight nanocomposites. The structure factors show well-dispersed, liquid-like particle structure. We see a decrease of the $S(0,\phi_c)$ value at low qD_c, implying a suppression of density fluctuations as ϕ_c is increased. Except at the highest volume fractions, there is no upturn in the scattering at low qD_c which supports that the particles are well dispersed. There is an increase in the magnitude of the first peak, $S(q^*,\phi_c)$, located at q^*D_c. This signifies that nearest-neighbor particle shells are becoming more coherent and agrees with the suppression of density fluctuations. In PEO2000, the peak steadily increases in magnitude, whereas the peak in PEO8000 and PEO20000 go through a maximum at $\phi_c \sim 0.25$. At higher ϕ_c the peak decreases in PEO8000 and PEO20000, meaning a loss of coherence in the nearest-neighbor shell. The structure in the three molecular weight nanocomposites at $\phi_c = 0.317$ appears to be the same despite the differences in structure at lower volume fractions. At $\phi_c = 0.317$, we see a rise in $S(0,\phi_c)$ which equates to an increase in large wavelength density fluctuations. An increase in long wavelength density fluctuations implies interparticle attractions. We note that these attractions appear to switch on when the position of the peak is still smaller than 2π, meaning the particles are not in direct contact.

Figure 12 shows a plot of $1/S(0,\phi_c)$, the inverse of the compressibility and $S(q^*,\phi_c)$, versus ϕ_c for PEO2000, PEO8000, and PEO20000. The graph also contains past data for PEO400 and PEO1000 as a comparison. The inset in Figure 12 contains results at low ϕ_c. We find the compressibility and $S(q^*)$ in the three lower molecular weight nanocomposites to be nearly identical at $\phi_c \sim 0.09$. When comparing the full structure factors, the microstructures appear to be the same for PEO400, PEO1000, and PEO2000 nanocomposites (Figure 13). This is surprising since viscosity measurements show an effective particle hydrodynamic diameter that increases with molecular weight. The particle structure factor in PEO20000 at $\phi_c \sim 0.09$ shows considerably more structure.

The similarity of the microstructure at $\phi_c \sim 0.09$ for PEO400, PEO1000, and PEO2000 nanocomposites suggests a difference in mechanical and thermodynamic behavior such that the hydrodynamic size from viscosity measurements does not determine the nanocomposite microstructure in the three lower molecular weight polymer melts.

A thermodynamic size of the particles is estimated by forcing a fit of the structure factor to a model hard sphere structure factor. Hard sphere structure factors are calculated using the Percus−Yevick closure through the method of Vrij and Baxter's simplification of the direct correlation function.[43−45] The model calculates the total scattering intensity of a suspension as a function of dimensionless scattering vector, qD, for an input volume fraction. A Gaussian particle size distribution is incorporated into the model to predict the scattering intensity of a polydisperse particle suspension. The silica particles are 10% polydisperse. Polydisperse structure factors are derived by dividing the total scattering intensity by the particle form factor.[44] The predictions of the model have been shown to predict the scattering intensity of polydisperse monomodal and bimodal particle populations.[46] Figure 14 shows a fit of PEO2000 at $\phi_c = 0.091$ to the model.

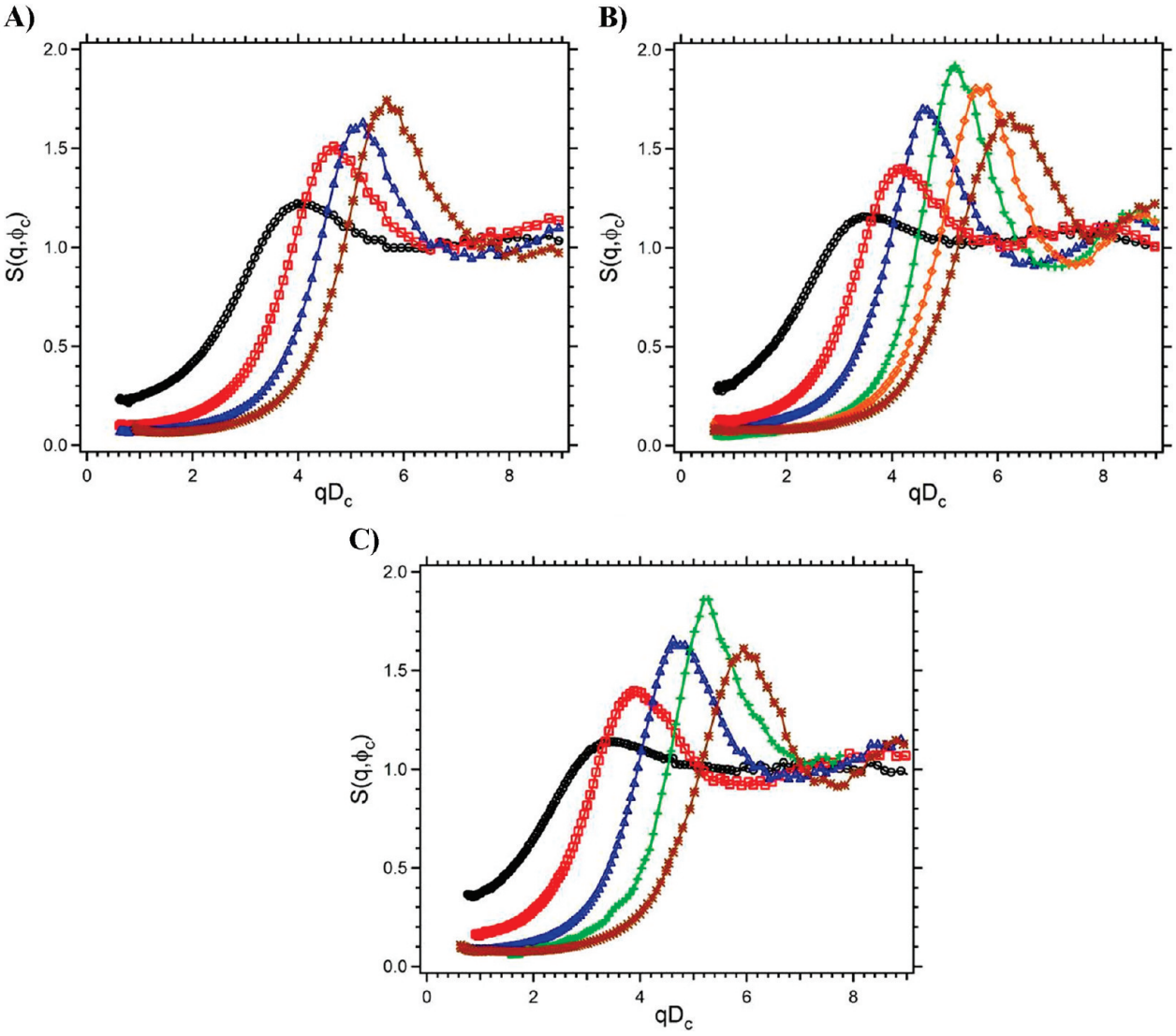

Figure 11. (A) Particle structure factors, $S(q,\phi_c)$, in PEO2000 at ϕ_c of 0.091 [○], 0.177 [□], 0.245 [△], and 0.317 [∗]. (B) Particle structure factors, $S(q,\phi_c)$, in PEO8000 at ϕ_c of 0.060 [○], 0.128 [□], 0.173 [△], 0.255 [+] 0.296 [◇], and 0.317 [∗]. (C) Particle structure factors, $S(q,\phi_c)$, in PEO20000 at ϕ_c of 0.052 [○], 0.096 [□], 0.173 [△], 0.255 [+], and 0.317 [∗].

The structure factors are fit to the model using two adjustable parameters: $\phi_{S(q)}$, an effective particle volume fraction, and D_{q^*}, a particle diameter that captures the average spacing between the particles. $\phi_{S(q)}$ captures the magnitudes of $S(0,\phi_c)$ and $S(q^*,\phi_c)$ in dimensionless scattering vector space. D_{q^*} transfers the model fit to dimensional scattering vector space. By allowing D_q* to be independent of $\phi_{S(q)}$, the model captures in a near-quantitative manner the experimental structure factors. Notice that D_{q^*} only shifts the data in q space but does nothing to the shape of the model structure factor. By forcing $S(0,\phi_c)$ to hard sphere values, we extract an effective thermodynamic volume fraction, $\phi_{S(q)}$. A thermodynamic size, $D_{S(q)}$, is extracted from $\phi_{S(q)}$: $D_{s(q)} = (\phi_{S(q)}/\phi_c)^{1/3}D_c$. Of significance is that the same value of $\phi_{S(q)}$ also predicts the magnitude of $S(q^*,\phi_c)$ and the shape of the first peak in $S(q,\phi_c)$ near q^*. This demonstrates that the structure can be interpreted in terms of effective hard sphere behavior.

The hydrodynamic and thermodynamic sizes are compared in Table 7. In the three lower molecular weight polymers, the hydrodynamic size, D_η, is smaller than the thermodynamic size, $D_{S(q)}$. The hydrodynamic size depends on molecular adsorption of polymer such that the particle carries a layer of polymer as the particle diffuses, yet the thermodynamic size in the three lower molecular weight nanocomposites is independent of molecular weight. PEO8000 and PEO20000 nanocomposites have a lower compressibility (higher $1/S(0,\phi_c)$) than the three lower molecular weight nanocomposites at low ϕ_c, resulting from particles having more structure. In these two nanocomposites, the thermodynamic size from the compressibility increases with molecular weight. (The thermodynamic size in PEO8000 was taken from fits of $S(q,\phi_c)$ at ϕ_c = 0.067 and 0.128, which both gave a size of 58 nm.) This suggests that the adsorbed layer may be contributing to the greater amount of particle structure in PEO8000 and PEO20000, but in the three lower molecular weight nanocomposites, interactions with a range that exceeds the adsorbed layer thickness are controlling the suspension microstructure.

As the volume fraction is increased, the compressibility of the dispersions in PEO400 and PEO1000 continues to decrease due to more intense structuring of the particles while the rate of change in reduction of the compressibility in PEO2000, PEO8000, and PEO20000 is diminished. The continued reduction of the compressibility in PEO400 and PEO1000 indicates that particles in these two melts remain

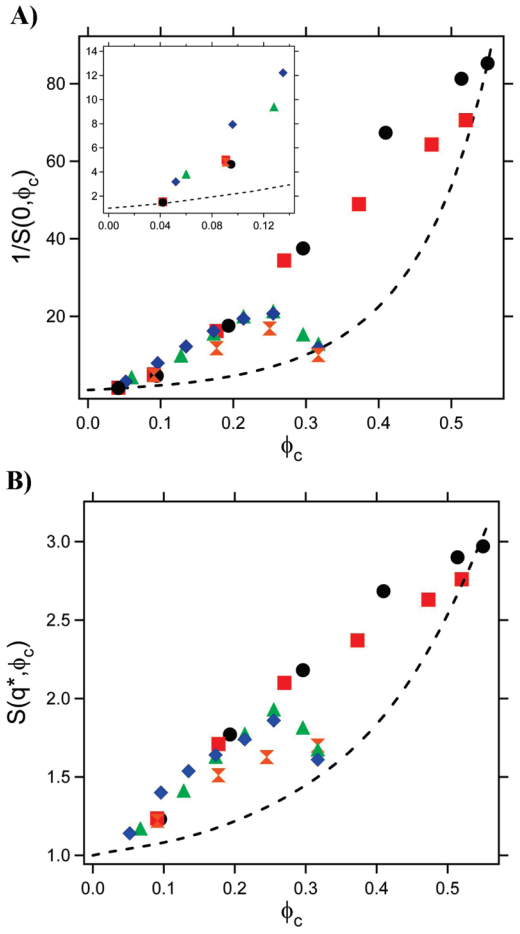

Figure 12. (A) Inverse compressibility, $1/S(0,\phi_c)$, plotted versus ϕ_c for PEO−silica nanocomposites in PEO molecular weight of 400 [●], 1000 [■], 2000 [solid ⧖], 8000 [▲], and 20000 [♦]. Inset is an enlarged view of the low ϕ_c inverse compressibility. (B) $S(q^*,\phi_c)$ is plotted versus ϕ_c for PEO−silica nanocomposites in PEO molecular weight of 400 [●], 1000 [■], 2000 [solid ⧖], 8000 [▲], and 20000 [◆].

stable up to and beyond volume fractions of 0.50. The similarity of the particle structure in PEO2000 with PEO400 and PEO1000 does not continue above $\phi_c \approx 0.09$ with PEO2000 nanocomposites having the least structure.

The particle microstructure in PEO20000 and PEO8000 nanocomposites become similar above $\phi_c \approx 0.20$. In PEO20000, $\phi_c/\phi_c^* < 1$ above $\phi_c \approx 0.20$, indicating that particle separations are comparable to the adsorbed layer thickness. As a result, increases in volume fraction must result in stripping of the polymer layer that appears to contribute to the greater structure in PEO20000 over PEO8000 and over the lower molecular weight nanocomposites.

At $\phi_c \approx 0.25$, the magnitude of the first structure peak, $S(q^*)$, in PEO8000 and PEO20000 decrease. This also corresponds to an increase in the compressibility. The structure in PEO2000 converges with the structure in PEO8000 and PEO20000 at $\phi_c = 0.317$. PEO2000 does not show a decrease in $S(q^*)$, but the magnitude of $S(q^*)$ at $\phi_{c,b}$ is similar for these three nanocomposites. These events point to the emergence of an attraction that is disrupting particle structure and increasing large wavelength particle density fluctuations. If this attraction is of sufficient magnitude, the upturn in $S(q)$ as q goes to zero may indicate that the particles are approaching a phase transition.

The observation of increased density fluctuations at low q correlates well with the observed change from ductile to brittle in the mechanical properties, thereby linking the change in the

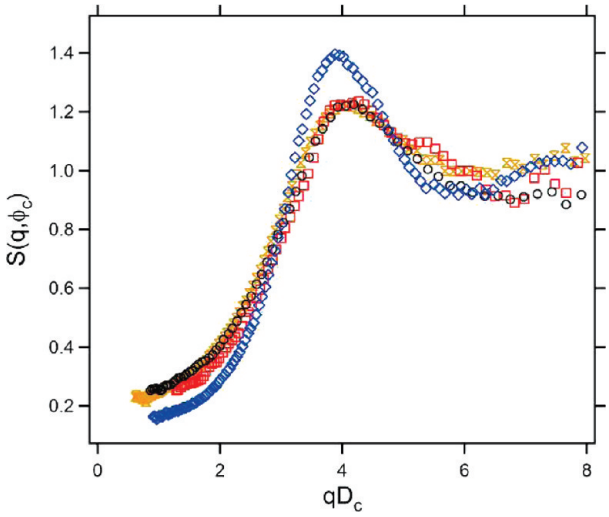

Figure 13. Particle structure factors, $S(q,\phi_c)$ versus the dimensionless scattering vector, qD_c, at $\phi_c \approx 0.09$ in PEO400 [○], PEO1000 [□], PEO2000 [⧖], and PEO20000 [◊].

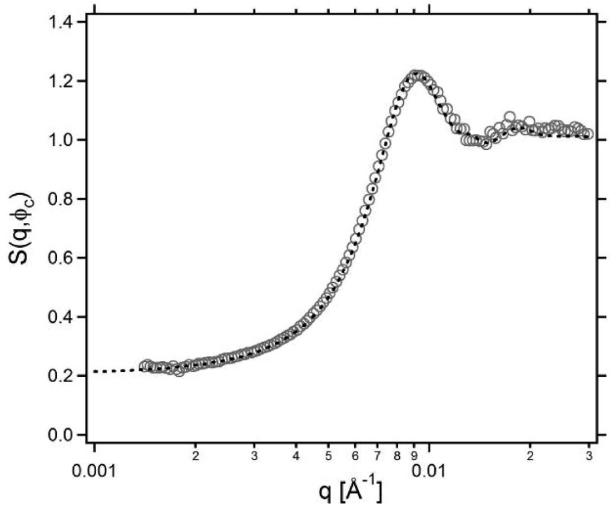

Figure 14. Particle structure factor in PEO2000 at ϕ_c of 0.091 [○]. The dashed line is a model fit to a hard sphere structure with a polydispersity of 10%. The model parameters are $\phi_{S(q)} = 0.21$ and $D_{q^*} = 64$ nm.

Table 7. Comparison of Particle Hydrodynamic Size and Thermodynamic Size in PEO Nanocomposites at $\phi_c \sim 0.09$

MW [g/mol]	D_η [nm]	$D_{S(q)}$ [nm]
400	46.4	57
1000	47.7	57
2000	49.3	57
8000	54.6	58
20 000	60.8	62

mechanical response to a change in particle stability. The similarity of the structure factors at this volume fraction suggests that the onset of attraction and resulting mechanical transition are insensitive to molecular weight. The mechanical properties of the nanocomposites are vastly different as this volume fraction is approached. PEO20000 is a rigid solid, PEO8000 is a soft solid, and PEO2000 is a liquid. The onset of brittle behavior occurs at average particle separations that are independent of ϕ_c^* and $\phi_{c,g}$. Incidentally, the volume fraction in PEO2000 never approaches these two volume fractions, $\phi_c^* = 0.410$ and $\phi_{c,g} = 0.413$, due to the intersection of the brittle transition at $\phi_{c,b} = 0.317$.

IV. Conclusion

We extract the following picture of the effect of polymer entanglements on nanocomposite rheology. Of significance to the conclusions discussed here are that they are focused on a system where the polymer adsorbs to the particle surface. Previous studies suggest the strength of attraction between a polymer segment and the polymer surface is modest and lines in the range of $0.3-0.5k_BT$.[47] Measurement of the low shear rate viscosity of particles suspended in entangled polymer melts reveals the influence of molecular weight and entanglements on nanocomposite flow properties. While adsorption of entangled polymers to the particle surface increases the particle hydrodynamic diameter in the same way as the unentangled polymers, a longer range interaction is also introduced that we associate with secondary entanglements. Thus, secondary entanglements affect particle−particle interactions, causing the particles to make a stronger contribution to the nanocomposite viscosity than when the suspending polymer is unentangled. At sufficiently low volume fractions, defined here as when $\phi_c/\phi_{c,e} < 1$, the average particle spacing is many times R_g, and the particles increase the bulk polymer viscosity without significant alteration of polymer entanglement dynamics. When ϕ_c is greater than $\phi_{c,e}$ but less than ϕ_c^*, the majority of polymer entanglements are secondary entanglements. Here ϕ_c^* is the volume fraction when the entanglements between adsorbed polymer chains become important, and this separation is associated with a change in frequency dependence of the low strain moduli and the appearance of two yield strains in the nonlinear moduli. As the volume fraction exceeds ϕ_c^*, there is a rapid rise in the low frequency moduli. At the same time, ϕ_c is approaching $\phi_{c,g}$ where unentangled nanocomposite melts displayed glassy particle dynamics. The linear moduli of the entangled nanocomposites do not show distinct glassy particle relaxations. The loss of glassy dynamics in these very dense nanocomposites results from the dominance of polymer relaxations in determining composite mechanical behavior.

The onset of two yield strains in the nonlinear rheology demonstrate that when $\phi_c/\phi_{c,e} < 1$, there is a two-step mechanism for structural rearrangement. Israelachvili and Kott show the emergence of an attractive well in the force profile of a confined polymer with molecular weight $\sim M_c$ as plates are pulled apart. This picture suggests that as an applied stress pulls particles apart, the entangled polymer trapped between particles resists flow of the nanocomposite. Thus, polymer that entangled between particles appears to simulate an attraction when the nanocomposite melt is subjected to an applied stress of increasing amplitude.

Under conditions where the confined polymers are entangled, the first yield strain in the nonlinear elastic modulus marks the transition from the linear viscoelastic regime at low strain to an intermediate strain softening regime. The first yield strain occurs at strains near 0.01−0.05 and is attributed to initial distortion of the particle microstructure. As particles are pulled away from neighbors, entanglements between particles hinder the exchange of neighbors and simulate an attraction. Shear of the polymer between particles accelerates the release of these entanglements which softens the nanocomposite. As the molecular weight of the polymer increases, each chain participates in more entanglements. This results in the shifting of the first yield to higher strain.

At the second yield, entanglements between particles are released and particles exchange neighbors. The second yield shifts to higher strain as the polymer molecular weight is increased. This is explained by primary and secondary entanglements being longer in range in higher molecular weight polymer. Core particles must move larger distances for the release of these entanglements between particles. The shifting of the second yield strain to lower strain with higher ϕ_c is caused by a reduction in the interparticle separation distance. As the interparticle separation is reduced, the microstructure is tightened and the core particles do not have to move as far to exchange neighbors. The lowering of the second strain is also influenced by stripping of adsorbed polymer as ϕ_c is increased. The frequency independence of the strain location of the second yield shows that the transition depends on the amount that the nanocomposite is distorted.

The appearance of strain hardening at the second yield strain is a unique feature of the stress sweeps and occurs as $\phi_c/\phi_c^* > 1$. Strain hardening is found in polymer networks where flow is restricted by chemical or physical constraints. As the polymer is confined to distances that characterize the thickness of the adsorbed layer such that adsorbed polymer occupies the same space, primary entanglements will dominate entanglement dynamics. Primary entanglements are more restricted than secondary entanglements since entanglements are between polymer that are both surface adsorbed. The dependence of strain hardening on the rate of strain ($\gamma\omega$) shows that the rearrangement of particles depends on the relaxation time of primary entanglements. A fast strain rate leads to significant strain hardening because primary entanglements cannot relax over the time scale of the strain frequency, whereas a slower strain frequency allows the entanglements time to respond to the stress and less strain hardening is seen. The relaxation time of primary and secondary entanglements will be unique for a particular entangled nanocomposite with a specific particle volume fraction and polymer molecular weight.

The transition to terminal flow at high strain occurs when confined entanglements release and the melt flows allowing particles to exchange neighbors. When the rate of strain is much faster than the time scale for the release of entanglements and the nanocomposites harden, the terminal transition at the apex of hardening is not entirely clear. The transition to terminal behavior may be the pulling out of entanglements. Ordering of segments occurs as friction between polymer chains resist entanglements from being pulled out. Therefore, the stress may speed up entanglement dynamics. In the PEO20000 nanocomposite at $\phi_c = 0.265$, the polymer is severely confined and the nanocomposite fractures as it is strained. Fracture occurs when the applied stress becomes too great for the confined entanglements to relieve the stress. It is highly unlikely that the fracture is due to the breaking of entanglements which would require chain scission. A more likely explanation is the debonding of segments from the particle surface.

There is a change in the nonlinear strain behavior of PEO8000 at $\phi_c = 0.317$ such that the nanocomposite becomes brittle and fractures as it is strained. The PEO20000 nanocomposites remain ductile as the polymer is confined to surface separations that exceed the PEO8000 nanocomposite at the ductile to brittle transition. There is also a loss of strain hardening behavior.

It has been seen that the addition of nanoparticles to a polymer matrix can cause an elevation in the polymer glass transition temperature, T_g, for polymer that preferentially adsorbs to the particle surface. The T_g behavior of PEO is rather unusual compared to most polymers where T_g typically increases with MW. The T_g of PEO peaks at a molecular weight of 6000 ($T_g = -17$ °C) and decreases thereafter reaching a high molecular weight limit of −53 °C.[48] This peculiar behavior of T_g for PEO may explain the brittle transition for PEO2000, PEO8000, and PEO20000 compared to PEO400 and PEO1000 where no transition is observed. This would still require a rather large increase in T_g to exceed the system temperature of 75 °C. Large increases in T_g have been reported in a few nanocomposite systems,[49,50] and confinement of polymer was shown to lead to a diverging elevation in T_g.[50] One potential issue with this interpretation is that the T_g for PEO2000, PEO8000, and PEO20000 is not constant, while the brittle transition for these three nanocomposites appears insensitive to molecular weight.

When comparing the ductile to brittle transition to the trends seen in the particle structure factor, the brittle transition is linked to an increase in particle density fluctuations. An increase in density fluctuations is a sign of particle instability and implies the proximity of a phase transition. As a second explanation, the change in the nonlinear strain behavior and the disruption of the microstructure may signal a polymer bridging transition where particles reach a critical separation distance such that a continuous string of PEO segments spans two particle surfaces. Our initial intuition tells us that we can expect bridging when the particle surface separation is of the order $2R_g$. This expectation of polymer bridging is not consistent with our results in that we see remarkable similarity between the particle microstructure independent of molecular weight, implying that the dispersions are moving toward a common instability point. At $\phi_{c,b} = 0.317$, the particle surface separation in terms of R_g are 6.0, 3.0, and 1.9 for PEO2000, PEO8000, and PEO20000, respectively.

Recent PRISM predictions of Hooper and Schweizer predict two types of particle instabilities depending on strength of the segment−surface interaction.[11,12] Weak adsorption yields depletion flocculation and strong adsorption yields bridging flocculation. Bridging flocculation is said to have a weak dependence on molecular weight. Our findings with regard to particle stability qualitatively agree with the predictions of Hooper and Schweizer, who predict that at modest to strong segment−surface interaction the particles will initially be stable at low ϕ_c and cross a bridging phase boundary at higher ϕ_c. They predict minor influence of molecular weight on the location of the bridging transition in terms of ϕ_c since particle stability is largely controlled on the polymer segment level rather than on the polymer molecule level.

Hooper and Schweizer predict that the particle−particle potential of mean force is oscillatory changing from overall attractive to overall repulsive based on the segment−surface interaction. The oscillations have a period of the segment size and amplitude that increases with molecular weight. For a strong segment−surface attraction, segments will resist, leaving the surface when confined between two particles. Yet, the oscillatory PMF allows particles to fall into potential wells farther away from the surface. The loss of particle stability indicated by the rise in $S(0,\phi_c)$ may be associated with particles falling into these potential wells when particles reach separations on the order of several PEO segments.

This description of the particle potential of mean force is not in agreement with our characterization of the particle pair interaction from dilute viscosity measurements. There we see a repulsion that scales on R_g and implies that an adsorbed polymer layer moves with the particles. We see the consequence of direct interaction of the adsorbed layers in entangled nanocomposites by the slowing down of entanglement dynamics. The formation of an adsorbed molecular layer is not predicted by equilibrium polymer adsorption for polymer melts and is assumed to be a consequence of pinning polymer segments to the surface.[51,52] Therefore, care should be used when attempting to understand particle stability in PEO in relation to equilibrium theories if particle stability is being influenced by an adsorbed layer. At the same time, we note that the particle surface separation in PEO2000 is always greater than $6R_g$ until $\phi_c = 0.317$ where the surface separation equals $6R_g$. Attributing the particle structure solely to the formation of an adsorbed molecular layer is also not sufficient in explaining the particle microstructure and particle stability.

To rationalize the features of our data that show a clear influence of polymer molecular weight with a phase transition that is independent of molecular weight, we suggest several ways to view the nanocomposite depending on the volume fraction of particles. At low ϕ_c, the polymer adsorbs to the particle surface and forms an adsorbed molecular layer with a thickness that scales on R_g. The formation of an adsorbed layer impacts the viscosity by causing polymer to diffuse with the particle. For low molecular weight PEO, the adsorbed layer does not control the structuring of particles in the polymer melt. Instead, the particle microstructure appears to be governed by the structuring of polymer segments adjacent to the surface. The structuring of segments has a minor impact on nanocomposite viscosity since unadsorbed polymer can move freely at the interface between adsorbed polymer and unadsorbed polymer. As the molecular weight of the polymer is increased such that the thickness of the adsorbed polymer extends beyond the structuring of segments away from the surface, the structure begins to be influenced by the adsorbed polymer which resists confinement. As the molecular weight of the nanocomposite increases above the entanglement molecular weight, entanglement dynamics influence the flow properties of the nanocomposite but should not influence the static structure. As ϕ_c is increased, secondary entanglements of free polymer with adsorbed polymer and primary entanglements between adsorbed layers impact the flow of the nanocomposite. As the surface separation reaches dimensions of a polymer molecule, the adsorbed polymer will have to adopt a new surface conformation. High molecular weight PEO will have to adjust its surface conformation to accommodate the confined dimension. When the surface separation is comparable to several PEO segments, we expect the molecular weight to have less influence on the particle microstructure. The particles will not be able to distinguish between different molecular weight of PEO because the polymer will appear as a sea of PEO segments. A segment bridging transition sets in when the particle surface separation reaches the length scale of several PEO segments. Particles hop over kinetic barriers and fall into potential wells. The consequence is a nanocomposite that looses ductility and becomes brittle.

Acknowledgment. SAXS data were collected at the X-ray Operations and Research beamline 8ID-E at the Advanced Photon Source (APS), Argonne National Laboratory. The APS is supported by the U.S. Department of Energy, Office of Science, Office of Basic Energy Sciences, under Contract DE-AC02-06CH11357. We appreciate our collaborative relationship and helpful discussions with Ken Schweizer and Lisa Hall. This work was supported by the Nanoscale Science and Engineering Initiative of the National Science Foundation under NSF Award DMR-0642573.

References and Notes

(1) Aranguren, M. I.; Mora, E.; DeGroot, J. V.; Macosko, C. W. *J. Rheol.* **1992**, *36* (6), 1165–1182.
(2) Mongruel, A.; Cartault, M. *J. Rheol.* **2006**, *50* (2), 115–135.
(3) Wang, M.-J. *Rubber Chem. Technol.* **1998**, *71* (3), 520.
(4) Zhang, Q.; Archer, L. A. *Langmuir* **2002**, *18* (26), 10435–10442.
(5) Zhu, Z. Y.; Thompson, T.; Wang, S. Q.; von Meerwall, E. D.; Halasa, A. *Macromolecules* **2005**, *38* (21), 8816–8824.
(6) Chazeau, L.; Brown, J. D.; Yanyo, L. C.; Sternstein, S. S. *Polym. Compos.* **2000**, *21* (2), 202–222.
(7) Sternstein, S. S.; Zhu, A. J. *Macromolecules* **2002**, *35* (19), 7262–7273.
(8) Granick, S.; Hu, H.-W. *Langmuir* **1994**, *10* (10), 3857–3866.
(9) Granick, S.; Hu, H.-W.; Carson, G. A. *Langmuir* **1994**, *10* (10), 3867–3873.
(10) Payne, A. R. *J. Appl. Polym. Sci.* **1962**, *6* (19), 57–63.
(11) Hooper, J. B.; Schweizer, K. S. *Macromolecules* **2005**, *38* (21), 8858–8869.
(12) Hooper, J. B.; Schweizer, K. S. *Macromolecules* **2006**, *39* (15), 5133–5142.
(13) Hooper, J. B.; Schweizer, K. S.; Desai, T. G.; Koshy, R.; Keblinski, P. *J. Chem. Phys.* **2004**, *121* (14), 6986–6997.
(14) Horn, R. G.; Israelachvili, J. N. *Macromolecules* **1988**, *21* (9), 2836–2841.

(15) Israelachvili, J. N.; Kott, S. J. *J. Chem. Phys.* **1988**, *88* (11), 7162–7166.
(16) Luengo, G.; Schmitt, F. J.; Hill, R.; Israelachvili, J. *Macromolecules* **1997**, *30* (8), 2482–2494.
(17) McGuiggan, P. M.; Gee, M. L.; Yoshizawa, H.; Hirz, S. J.; Israelachvili, J. N. *Macromolecules* **2007**, *40* (6), 2126–2133.
(18) Van Alsten, J.; Granick, S. *Macromolecules* **1990**, *23* (22), 4856–4862.
(19) Roberts, C.; Cosgrove, T.; Schmidt, R. G.; Gordon, G. V. *Macromolecules* **2001**, *34* (3), 538–543.
(20) Dreiss, C. A.; Cosgrove, T.; Benton, N. J.; Kilburn, D.; Alam, M. A.; Schmidt, R. G.; Gordon, G. V. *Polymer* **2007**, *48* (15), 4419–4428.
(21) Shim, S. E.; Isayev, I.; Meerwall, E. V. *J. Polym. Sci., Part B: Polym. Phys.* **2003**, *41* (5), 454–465.
(22) Ozisik, R.; Zheng, J.; Dionne, P. J.; Picu, C. R.; von Meerwall, E. D. *J. Chem. Phys.* **2005**, *123* (13).
(23) Berriot, J.; Lequeux, F.; Monnerie, L.; Montes, H.; Long, D.; Sotta, P. *J. Non-Cryst. Solids* **2002**, *307*, 719–724.
(24) Arrighi, V.; Higgins, J. S.; Burgess, A. H.; Floudas, G. *Polymer* **1998**, *39* (25), 6369–6376.
(25) Anderson, B. J.; Zukoski, C. F. *Macromolecules* **2008**, *41* (23), 9326–9334.
(26) Anderson, B. J.; Zukoski, C. F. *J. Phys.: Condens. Matter* **2009**, *21* (28), 285102.
(27) Stöber, W.; Fink, A.; Bohn, E. *J. Colloid Interface Sci.* **1968**, *26* (1), 62–69.
(28) Kugler, J.; Fischer, E. W.; Peuscher, M.; Eisenbach, C. D. *Makromol. Chem.* **1983**, *184* (11), 2325–2334.
(29) Anderson, B. J.; Zukoski, C. F. *Macromolecules* **2007**, *40* (14), 5133–5140.
(30) George, A.; Wilson, W. W. *Acta Crystallogr., Sect. D* **1994**, *50*, 361–365.
(31) Kulkarni, A. M.; Chatterjee, A. P.; Schweizer, K. S.; Zukoski, C. F. *Phys. Rev. Lett.* **1999**, *83* (22), 4554–4557.
(32) Rosenbaum, D.; Zamora, P. C.; Zukoski, C. F. *Phys. Rev. Lett.* **1996**, *76* (1), 150–153.
(33) Rosenbaum, D. F.; Zukoski, C. F. *J. Cryst. Growth* **1996**, *169* (4), 752–758.
(34) Graessley, W. W. *J. Chem. Phys.* **1967**, *47* (6), 1942–1953.
(35) Larson, R. G. *The Structure and Rheology of Complex Fluids*; Oxford University Press: New York, 1999.
(36) Montfort, J. P.; Hadziioannou, G. *J. Chem. Phys.* **1988**, *88* (11), 7187–7196.
(37) Cichocki, B.; Felderhof, B. U. *J. Chem. Phys.* **1988**, *89* (6), 3705–3709.
(38) Anderson, B. J.; Zukoski, C. F. *J. Phys.: Condens. Matter* **2009**, submitted.
(39) Fetters, L. J. D. J. L.; Colby, R. H. Chain Dimensions and Entanglement Spacings. In *Physical Properties of Polymers Handbook*; Springer: New York, 2007; pp 447−454.
(40) Russel, W. B.; Saville, D. A.; Schowalter, W. R. *Colloidal Dispersions*; Cambridge University Press: Cambridge, UK, 1992.
(41) Hoy, R. S.; Robbins, M. O. *J. Polym. Sci., Part B: Polym. Phys.* **2006**, *44* (24), 3487–3500.
(42) Hoy, R. S.; Robbins, M. O. *Phys. Rev. E* **2008**, *77* (3), 031801.
(43) Baxter, R. J. *J. Chem. Phys.* **1970**, *52* (9), 4559–4562.
(44) van Beurten, P.; Vrij, A. *J. Chem. Phys.* **1981**, *74* (5), 2744–2748.
(45) Vrij, A. *J. Chem. Phys.* **1979**, *71* (8), 3267–3270.
(46) Anderson, B. J.; Gopalakrishnan, V.; Ramakrishnan, S.; Zukoski, C. F. *Phys. Rev. E* **2006**, *73* (3), 031407–13.
(47) Hall, L. M.; Anderson, B. J.; Zukoski, C. F.; Schweizer, K. S. *Macromolecules* **2009**, DOI: 10.1021/ma901523w.
(48) Faucher, J. A.; Koleske, J. V.; E. R. Santee, J.; Stratta, J. J., C. W. W. III *J. Appl. Phys.* **1966**, *37* (11), 3962−3964.
(49) Priestley, R. D.; Ellison, C. J.; Broadbelt, L. J.; Torkelson, J. M. *Science* **2005**, *309* (5733), 456–459.
(50) Rittigstein, P.; Priestley, R. D.; Broadbelt, L. J.; Torkelson, J. M. *Nat. Mater.* **2007**, *6* (4), 278–282.
(51) de Gennes, P. G. *C. R. Acad. Sci. Paris* **1987**, *305*, 1181.
(52) Horn, R. G.; Hirz, S. J.; Hadziioannou, G.; Frank, C. W.; Catala, J. M. *J. Chem. Phys.* **1989**, *90* (11), 6767–6774.
(53) Cheng, Z.; Zhu, J.; Chaikin, P. M.; Phan, S.-E.; Russel, W. B. *Phys. Rev. E* **2002**, *65*, 041405.